Spectroscopy of Eu^{3+} ions in congruent strontium barium niobate crystals

Ä. Andresen, A.-N. Bahar, D. Conradi, I.-I. Oprea, R. Pankrath, U. Voelker, K. Betzler,* and M. Wöhlecke
Fachbereich Physik, Universität Osnabrück, D-49069 Osnabrück, Germany

U. Caldiño,† E. Martín, D. Jaque, and J. García Solé
Departamento de Física de Materiales, C-IV, Universidad Autónoma de Madrid, 28049 Cantoblanco (Madrid), Spain
(Received 11 February 2008; revised manuscript received 23 April 2008; published 9 June 2008)

The optical properties of single crystals of strontium barium niobate, grown from the congruently melting composition and doped with different amounts of europium, are investigated. Absorption and emission spectra are measured in the visible and infrared spectral regions at different temperatures. From the spectra, conclusions on the structural sites can be drawn, revealing the major occupations of the B1 and B2 sites, and a minor one of the A2 site. The data are used to calculate crystal-field parameters for the mainly occupied site. A Judd–Ofelt analysis shows that the radiative quantum efficiency is approximately 70%. Furthermore, the influence of europium doping on the phase-transition temperature is determined.

DOI: 10.1103/PhysRevB.77.214102 PACS number(s): 77.84.Dy, 71.55.Ht, 78.55.Hx

I. INTRODUCTION

Due to its interesting nonlinear optic, electro-optic, photorefractive, and dielectric properties, the solid solution strontium barium niobate, $Sr_xBa_{1-x}Nb_2O_6$—henceforth denoted as SBN—has gained considerable interest for potential applications. These include pyroelectric detection,[1] surface acoustic wave devices,[2] electro-optic modulation,[3] holographic data storage,[4] phase conjugation,[5] quasi-phase-matched optical frequency doubling,[6] and the generation of photorefractive solitons.[7]

SBN crystallizes in tetragonal tungsten bronze structure over a wide solid solution range, the existence region of this tetragonal phase had been recently determined[8] to be $0.32 \leq x \leq 0.82$. Throughout this tetragonal phase, SBN is ferroelectric at low temperatures (point group, 4 mm) and paraelectric at high temperatures (point group, 4/m mm). The Curie temperatures vary from 290 ($x=0.82$) to 500 K ($x=0.32$).[9]

Dopants have been shown to modify the properties of SBN distinctly. Thus, e.g., the Curie temperature can be greatly varied by doping with cerium and chromium.[10] To date, however, only few is known about luminescent dopants in SBN. Such dopants could be used to tailor the fluorescence properties of SBN for applications as, for instance, self-frequency converter laser materials.[11]

Several investigations have been performed on trivalent lanthanide ions (see, e.g., Refs. 12–16). One of the most interesting of these trivalent dopants is europium, Eu^{3+}, on which our present investigations will concentrate.

Eu^{3+} is known as an efficient red phosphor widely used in color cathode-ray tubes. As its optical properties are determined by the *f*-shell electrons, which are only slightly influenced by the environment, it can also be used in crystals as an efficient fluorescence dopant. Besides its interesting luminescence properties, Eu^{3+} ions are excellent optical probes because of the relative simplicity of its energy-level structure and the single degeneracy of both the initial states for absorption ($^7F_0$) and emission ($^5D_0$).

Still an open question is the preferred structural site, on which Eu^{3+} ions are incorporated (see, for instance, Refs. 15 and 16). Concerning their ionic radius, Eu^{3+} ions would be fitting into any of four different sites in the crystal frame of SBN including A1—partially occupied by Sr ions, A2—partially occupied by Sr or Ba ions, and B1 and B2—both occupied by Nb ions.

In this paper, we will present comprehensive experimental results on Eu^{3+} in SBN concerning distribution coefficients, influence on the phase transition, and optical absorption and emission. In addition, some implications are derived—site occupancies, energy levels, crystal-field parameters, Judd–Ofelt parameters, emission rate, and quantum yield.

II. CRYSTAL GROWTH AND PREPARATION

The crystals for our investigations were grown from the congruently melting composition of SBN ($Sr_xBa_{1-x}Nb_2O_6$ with $x=0.61$) using the Czochralski technique. Details of the growth process are described in Ref. 8. Eu_2O_3 was added to the melt in a series ranging from 0 to 2 mol %. To determine the crystal composition and the distribution coefficient for europium between melt and crystal, accurate x-ray fluorescence spectra were measured and evaluated (for details of the measurement and the evaluation procedure, see Ref. 8).

Our measurements revealed a distribution coefficient,

$$d = c_{\mathrm{Eu}}^{\mathrm{crystal}}/c_{\mathrm{Eu}}^{\mathrm{melt}} = 0.57 \pm 0.02, \tag{1}$$

which turned out to be approximately constant within our doping range. Throughout this paper we will characterize the samples by their solid composition, i.e., the europium content in the crystal, expressed as molar percentage of Eu per Nb or—which is accordingly equal—as molar percentage of Eu_2O_3 per $Sr_xBa_{1-x}Nb_2O_6$.

The crystal structure of SBN is tetragonal with point symmetry 4/m mm in the unpolar paraelectric high-temperature phase and with point symmetry 4 mm in the polar ferroelectric low-temperature phase, respectively. Thus the crystals are optically uniaxial in both phases with the crystallographic *c* axis being the optical axis. For the optical measurements, therefore, samples were cut to a typical size of 5^*5^*5 mm^3, precisely oriented with respect to the crystallo-

graphic axes, and polished to optical quality. The measurements, thus, could be performed in all three essential geometric configurations for optically uniaxial crystals:

(i) $\boldsymbol{\alpha}$: Light propagation parallel to the crystallographic c axis and light polarization perpendicular to the c axis.

(ii) $\boldsymbol{\pi}$: Light propagation perpendicular to the crystallographic c axis and light polarization parallel to the c axis.

(iii) $\boldsymbol{\sigma}$: Light propagation perpendicular to the crystallographic c axis and light polarization perpendicular to the c axis.

III. EXPERIMENT RESULTS

A. Phase transition temperature as a function of Eu doping

Dopants are known to influence the transition temperature region from the paraelectric to the ferroelectric phase of SBN distinctly. This previously was found, e.g., for doping with cerium or chromium.[10,17]

Usually this transition temperature is defined by direct pyroelectric measurements of the polarization decay when heating previously poled samples.[9] To measure this transition temperature, however, both on heating *and* cooling, we applied optical second-harmonic measurements on unpoled samples yielding the temperature dependence of the second-harmonic intensity $I_{\mathrm{SHG}}(T)$. As fundamental light source, a pulsed Nd:yttrium aluminum garnet (YAG) laser was used (with repetition rate of 20 Hz, pulse width of 5 ns, and pulse energy of 50 mJ). The sample heating and cooling rate during the measurements was approximately 40 K/h.

The second-harmonic intensity is proportional to the square of the effective tensor element of the second-order nonlinear susceptibility, which in turn is proportional to the ferroelectric polarization,

$$I_{\mathrm{SHG}}(T) \propto d_{\mathrm{eff}}^2(T) \propto P^2(T). \tag{2}$$

Thus from the second-harmonic measurements, the temperature dependence of the ferroelectric polarization $P(T)$ for heating and cooling can be derived. The inflection point T_i of this temperature dependence usually is regarded to define the transition temperature or (better) transition region (Curie region) in a relaxor ferroelectric.[10]

The results of these measurements are summarized in Fig. 1. The thus defined transition temperatures T_i depend linearly on the europium concentration c_{Eu} both for heating and cooling

$$T_{i,\mathrm{up}} = -35.7c_{\mathrm{Eu}} + 351.2, \tag{3}$$

$$T_{i,\mathrm{dn}} = -47.9c_{\mathrm{Eu}} + 349.2 \quad (c_{\mathrm{Eu}} \text{ in mol \%}, \quad T_i \text{ in K}). \tag{4}$$

The phase transition is strongly shifted to lower temperatures by the Eu doping. The results further show that the difference between $T_{i,\mathrm{up}}$ and $T_{i,\mathrm{dn}}$ increases with the europium content (temperature difference between the two fits in Fig. 1). This indicates a respective broadening of the phase transition's hysteresis with higher doping, i.e., a considerable increase in the relaxor behavior. Thus europium, besides affecting the optical properties, turns out to be an effective tool for tailoring the phase transition of SBN.

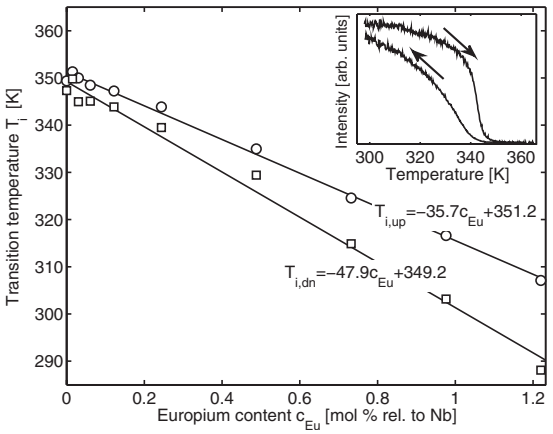

FIG. 1. Transition temperature T_i (i.e., inflection point) of the ferroelectric polarization as a function of the europium content in SBN. Circles: heating; squares: cooling. The lines are linear fits to the experimental data. In the inset a typical measurement of the heating and cooling behaviors is shown.

IV. ABSORPTION SPECTRA

Polarized optical-absorption measurements in the visible and near-infrared spectral regions were performed using a Bruins Instruments Omega 10 spectrometer. The wavelength accuracy of the instrument is approximately 0.1 nm in the visible region and 0.5 nm in the infrared region. The spectra were measured with 0.6 nm resolution in the visible region and approximately 12 nm resolution in the infrared region, respectively. The sample temperature could be varied between 10 and 300 K using a closed-cycle cooling system.

Figure 2 shows the europium absorption lines in the visible region for the three relevant polarizations, $\boldsymbol{\alpha}$, $\boldsymbol{\pi}$, and $\boldsymbol{\sigma}$, measured at a temperature of 300 K in a crystal with an Eu concentration of 0.98 mol %. The absorption lines are labeled each with the respective electronic transitions involved. The assignments are made according to the data for the free-ion energy-level scheme of Eu^{3+} measured by Carnall *et al.*[18] and to the data of the rare-earth-ion energy levels

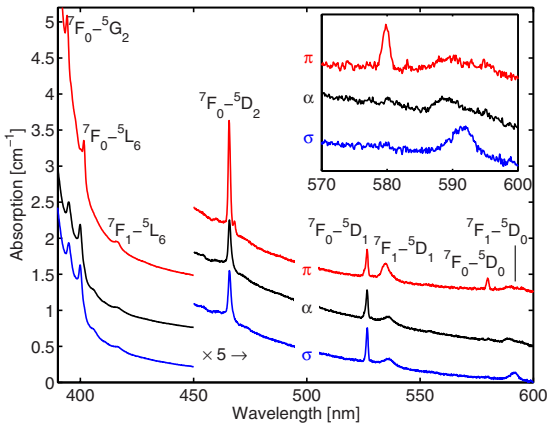

FIG. 2. (Color online) Absorption lines of europium ions in SBN in the visible spectral region for the three polarizations $\boldsymbol{\alpha}$, $\boldsymbol{\pi}$, and $\boldsymbol{\sigma}$ at a temperature of 300 K. In the inset the region of the transitions $^7F_0$, $^7F_1 \Rightarrow {}^5D_0$ is magnified.

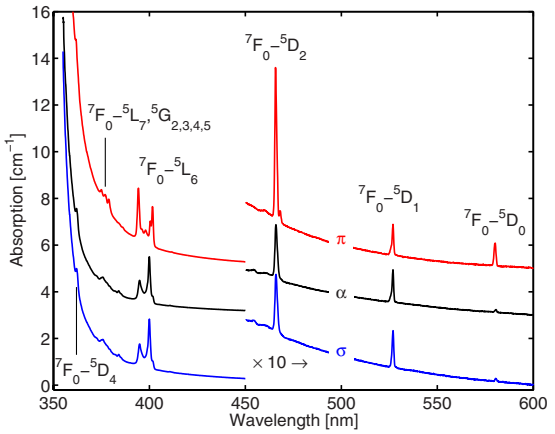

FIG. 3. (Color online) Absorption lines of europium ions in SBN in the visible spectral region for the three polarizations $\boldsymbol{\alpha}$, $\boldsymbol{\pi}$, and $\boldsymbol{\sigma}$ at a temperature of 10 K.

given by Dieke.[19] Because of its close proximity to the ground state $^7F_0$, the first-excited state $^7F_1$ is thermally populated at room temperature. Thus various transitions originating from $^7F_1$ are visible in the room-temperature absorption spectrum.

It should be already noted here that the transition $^7F_0 \Rightarrow {}^5D_0$ is only visible in the $\boldsymbol{\pi}$-polarized spectrum. This will allow important conclusions on the site symmetry of the europium ion (see Sec. V A). From the polarization properties of the spectra, one can further derive that the transition $^7F_1 \Rightarrow {}^5D_0$ shows an expressed magnetic dipolar behavior. All other transitions seem to be of dominantly electric dipolar character without any peculiarities.

To check the level assignments—especially those involving the $^7F_1$ level—and to get more information about the short-wavelength transitions, we additionally measured the absorption spectra at 10 K. The band edges are known to be shifted by more than 20 nm to the UV region when the temperature is changed from room temperature to below 50 K.[20] The low-temperature spectra for the visible region are shown in Fig. 3. All lines due to transitions originating from $^7F_1$ are now absent and additional near-UV transitions are found.

In the near-infrared spectral region, the transition from $^7F_0$ and $^7F_1$ to the $^7F_6$ level could be detected. Again, due to the temperature dependent occupation of the $^7F_1$ level, the transition originating thereof is missing at low temperatures. The spectra for 300 and 10 K, respectively, are sketched in Fig. 4.

Measurements on crystals with different Eu concentrations revealed a strictly linear dependence of the absorbance on concentration, even up to the highest doping levels. No saturation effects could be found. Moreover, the line shapes, too, did not show any dependence on the Eu concentration.

A. Luminescence spectra

Emission spectra due to transitions starting from the $^5D_0$ level were measured using a 532 nm frequency-doubled Nd:YAG laser as excitation source and a 0.75 m monochromator in combination with a photon counting system for detection.

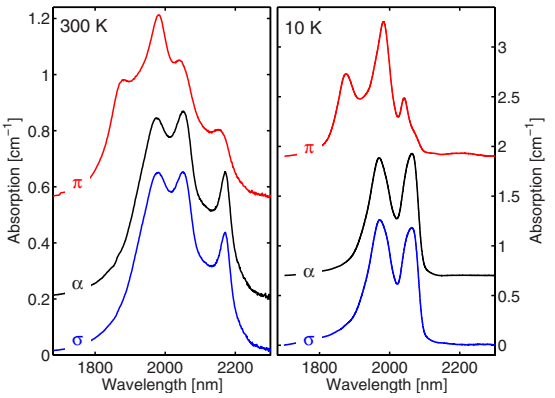

FIG. 4. (Color online) Absorption lines of europium ions in SBN in the infrared spectral region originating from the transitions $^7F_0$, $^7F_1 \Rightarrow {}^7F_6$ for the three polarizations $\boldsymbol{\alpha}$, $\boldsymbol{\pi}$, and $\boldsymbol{\sigma}$ at a temperature of 300 (left) and 10 K (right), respectively. In the low-temperature spectrum the transition originating from $^7F_1$ near 2200 nm is missing due to the low occupation of this level at low temperature.

The room-temperature spectra for the three polarizations are compared in Fig. 5. Features already suspected from the absorption spectra also show up in the luminescence spectra:

(1) The emission due to the transition $^5D_0 \Rightarrow {}^7F_0$ is strictly $\boldsymbol{\pi}$ polarized.

(2) The transition $^5D_0 \Rightarrow {}^7F_1$ shows expressed magnetic dipolar behavior.

To get, in addition, an overview over the higher ^5D states, luminescence spectra were measured using a semiconductor laser source at 390 nm for excitation. This excitation gives rise to a transient occupation of the higher ^5D states, result-

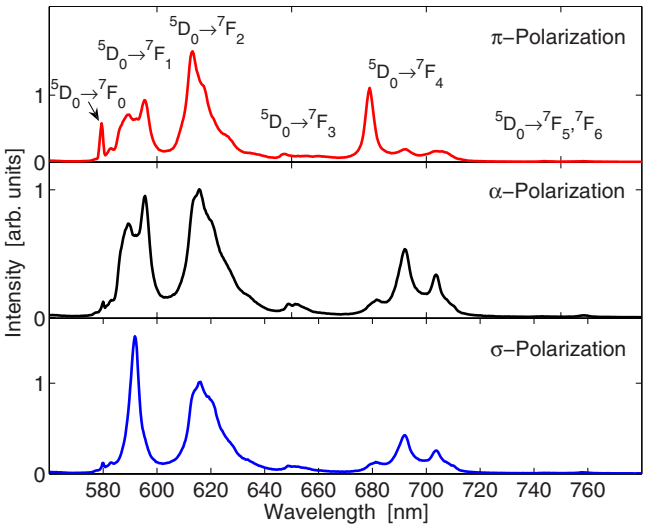

FIG. 5. (Color online) Emission spectra of europium ions in SBN at room temperature for the three relevant polarizations $\boldsymbol{\alpha}$, $\boldsymbol{\pi}$, and $\boldsymbol{\sigma}$. The vertical scalings for the three polarizations are given in corresponding arbitrary units. For a better comparison, α polarization was measured using a polarizer, too. Omitting it would yield an intensity more than twice as high.

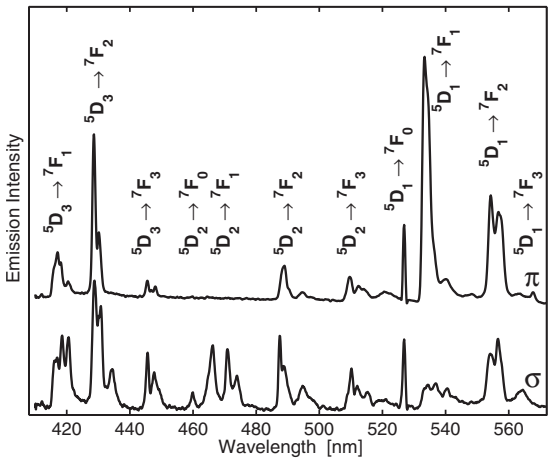

FIG. 6. Emission spectra of europium ions arising from transiently occupied higher ^5D states in SBN measured at a temperature of 20 K for the two polarizations $\boldsymbol{\pi}$ (upper spectrum) and $\boldsymbol{\sigma}$ (lower spectrum). The intensity scales are approximately equal for both spectra; compared to Fig. 5, the intensities here are lower by a factor of 50.

ing in extremely weak emission bands connected with transitions to ^7F states thereof. Figure 6 shows these spectra for π and σ polarizations.

All energy levels derived from the absorption and the emission lines, so far, are used for the theoretical evaluation of the energy parameters for the system SBN:Eu and are summarized in the respective chapter (see Table III).

Compared to the room-temperature spectra of Fig. 5, the according low-temperature emission spectra show up the same lines in nearly all region, although slightly narrower and more expressed. In the region of the $^5D_0 \Rightarrow {}^7F_0$, $^7F_1$ transitions, however, additional distinct lines appear in the low-temperature emission spectra, which are extremely narrow (half widths less than 0.5 nm) compared to all other lines. These lines are most expressed in the π-polarized emission. These additional lines are shown in Fig. 7, one in the region of the $^5D_0 \Rightarrow {}^7F_0$ and three near the $^5D_0 \Rightarrow {}^7F_1$ transition. For the other transitions, probably due to their wider multiplet splitting, it was not possible to resolve such additional lines.

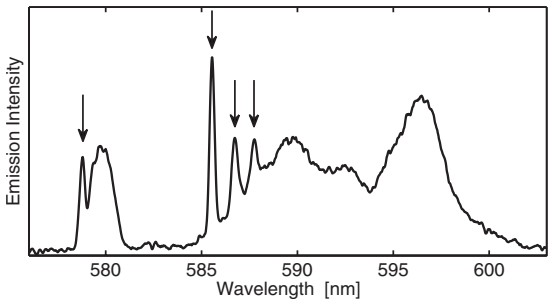

FIG. 7. Additional lines in the low-temperature emission spectra. The π-polarized emission is shown and the additional lines are marked by arrows. Compared to Fig. 5, the spectrum is measured under quite different conditions, thus, the intensities cannot be compared. The measured lifetimes (see following section), however, show that the total quantum yield is practically the same.

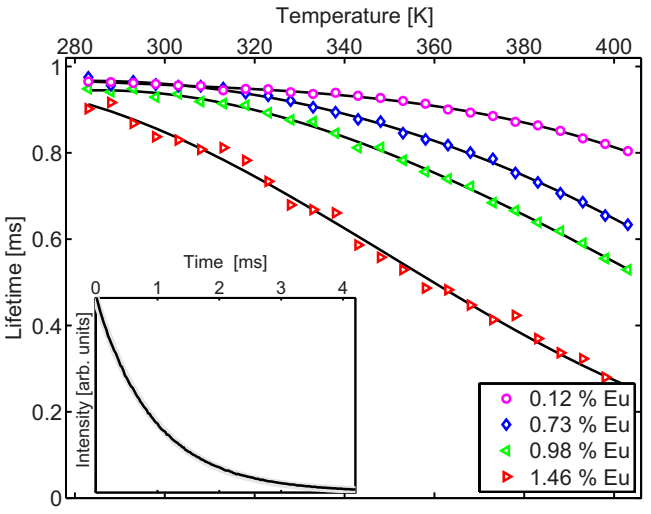

FIG. 8. (Color online) Temperature dependence of the total lifetime of the $^5D_0$ level for different Eu concentrations around the phase-transition region. In the inset a typical measurement is shown (black line) together with the respective exponential fit (gray).

B. Lifetimes

The total lifetime of the starting level $^5D_0$ for the emission lines was measured using pulsed excitation at 532 nm and photon counting techniques. Measuring at different spectral positions of the broader lines, we could detect a very small variation of the lifetime with a total variation (full width of the distribution) of approximately 7%. This is a hint that the respective site experiences different environments. However, no clear assignment to only few environments could be stated, thus, a larger number of different environments must be assumed (see discussion in Sec. IV A).

Due to this, we restricted our investigations to the several line centers selected of the broader lines starting at $^5D_0$. All these measurements showed a strictly exponential decay of the intensity with a time constant unique for certain europium concentration and temperature but irrespective of the final state of the transition. This exponential behavior was verified in a temperature range from 10 to 400 K for all europium concentrations investigated (0.1–1.5 mol %). We further found that the narrow lines (see Fig. 7), which we only could detect in the low-temperature spectra, show a lifetime that is approximately 10% larger than the average one of the broad lines.

For the broader lines for all compositions, nearly the same lifetime of approximately 1 ms was found up to the phase-transition region. This indicates that nonlinear effects such as excited-state absorption or energy-transfer upconversion do not affect the lifetimes—not even at high doping levels. For temperatures above the phase transition, however, the lifetimes decrease considerably. The results for temperatures above the phase-transition regions are summarized in Fig. 8. The effect of the phase transition on the lifetime for the respective concentrations (see Fig. 1) is obvious for all concentrations plotted. An intrinsic temperature quenching of the europium ions as an explanation for this decrease in lifetime can be excluded. Measurements of the temperature de-

TABLE I. Symmetries and expected radiative dipole transitions for the four possible structural sites in which Eu^{3+} could be incorporated in SBN.

Site	Symmetry	$^5D_0-^7F_0$ (ED)	$^5D_0-^7F_1$ (MD)
A1	C_4	1π	1π, 1σ
A2	C_s	$1(\pi,\sigma)$	1π, $2(\pi,\sigma)$
B1	C_{2v}	1π	2π,1σ
B2	C_1	$1(\pi,\sigma)$	$3(\pi,\sigma)$

pendence of the lifetime of the $^5D_0$ level of Eu^{3+} in Y_2O_3 (Ref. 21) show that in this persistent environment, the lifetime is constant ($\approx$1 ms) up to 800 K.

V. THEORY EVALUATIONS

A. Site symmetry

For the inclusion of Eu^{3+} ions in the crystal frame of SBN, four different sites are available: A1, A2, B1, and B2, whereas site C is regarded as being too small for the inclusion of such ions (for a detailed description of the crystal structure, see, for instance, Refs. 22–24). A1, surrounded by 12 oxygen ions, is partly occupied by Sr, A2, surrounded by 15 oxygen ions, partly by Sr or Ba, and both B1 and B2, surrounded by slightly distorted oxygen octahedra, are usually occupied by Nb. The local symmetries of these sites are listed in Table I together with the multiplicities and polarizations to be expected for the electric-dipole (ED) $^5D_0-^7F_0$ and the magnetic-dipole (MD) $^5D_0-^7F_1$ transitions of europium.

The comparison with the experimental spectra shows that B1 must be assumed to be the site mainly occupied by Eu^{3+} ions. Only this is compatible with the basic polarization properties of the spectra. However, in the absorption and emission spectra, both minor intensities for the $^5D_0-^7F_0$ transition are also measured for $\boldsymbol{\sigma}$ polarization. This indicates the occupation of additional sites. As these lines are lying at practically the same energies as the main lines, a similar environment for Eu^{3+}, as for the B1 sites, must be assumed. This is a strong indication for B2 sites, as approximately the same Eu-O distances therein as for B1 sites are in effect, leading to a similar crystal-field shift.

The relatively large widths of the main lines ($\approx$2 nm for the $^5D_0-^7F_0$ transition centered at 580 nm) suggest that either more than the two sites, B1 and B2, are involved or that these sites experience different environments in the crystal lattice. A closer look on the crystal structure of SBN yields the explanation. $Sr_xBa_{1-x}Nb_2O_6$ crystallizes in a so-called unfilled tungsten bronze structure with an intact frame structure consisting of slightly distorted oxygen octahedra. Two different sites at the centers of these octahedra, B1 and B2, are usually occupied by Nb ions. The Sr and Ba ions, however, don't completely fill this frame structure: on average, five of these ions are distributed among six sites, two for A1 and four for A2. X-ray diffraction measurements[24] have shown—for the crystal composition we used here (x=0.61)—that 72% of the A1 sites and 41% of A2 the sites are occupied by Sr, 48% of the A2 sites by Ba, and the remaining sites remain unoccupied. For the B1 sites, the nearest-neighbor shell is intact, consisting of six oxygens. The second-nearest-neighbor shell, however, contains four A2 sites. Considering the site symmetry, this yields 45 different combinations of Sr-occupied, Ba-occupied, and empty sites, all causing (at least slightly) different crystal fields. Their statistical weight spans from 0.014% (all surrounding A2 empty sites) to 9.2% (two different configurations of three Ba and one Sr). The purely statistical distribution, however, might be modified due to thermodynamic reasons during crystal growth. For the B2 sites, the situation is even more complicated. There are, in addition to the four A2 sites, two A1 sites in the second-nearest-neighbor shell. Furthermore, the symmetry of B2 is lower than that of B1. This yields 324 different combinations of Sr-occupied, Ba-occupied, and empty A sites around B2. This variation in the second-nearest-neighbor environment of the B1 and B2 sites, due to the *intrinsic* statistical disorder typical for the *unfilled* tungsten bronze structure, explains the relatively large width of the corresponding lines. It also explains why this large linewidth persists down to low temperatures: the crystal-field variation due to statistical disorder should not depend on temperature. In contrast to the B1 and B2 sites, the A1 and A2 sites are surrounded by the intact frame structure of NbO_6 octahedra without any intrinsic variation in the second-nearest-neighbor shell. For A sites, therefore, no inhomogeneous broadening of the lines is to be expected (see also Sec. IVC).

Complementary to our present results, recent extended x-ray-absorption fine structure measurements show that in SBN crystals grown at lower temperature by spontaneous nucleation in a flux, Eu^{3+} ions mainly occupy A1 sites.[25] This indicates that the favored structural site distinctly depends on the temperature at which the thermodynamic equilibrium is established. In crystals slowly grown at higher temperatures, the B1 sites are favored, whereas in crystals grown faster at lower temperatures, the thermodynamic equilibrium seems to be shifted toward the A1 sites.

B. Energy levels

The *optical* transitions in the electronic structure of Eu^{3+} occur within the energy levels of the $4f$ shell filled with 6 electrons ($4f^6$ structure). These energy levels are only slightly influenced by the crystalline environment. Thus, the influence of the crystal field can be treated as a small perturbation to the free-ion energy levels.

The total effective-operator Hamiltonian for the free-ion energy levels usually is written as[26]

$$\mathcal{H}_{\mathrm{FI}} = E_{\mathrm{avg}} + \sum_{k=2,4,6} F^k f_k + \zeta_{nl} A_{\mathrm{SO}}(nl) + \alpha L(L+1) + \beta G(G_2) + \gamma G(R_7) + \sum_{i=2,3,4,6,7,8} T^i t_i + \sum_{i=0,2,4} M^i m_i + \sum_{i=2,4,6} P^i p_i. \quad (5)$$

Therein the first three terms denote Coulomb and spin-orbit interactions. The α, β, and γ terms are corrections due to

two-electron operators, β and γ being associated with $G(G_2)$ and $G(R_7)$, the eigenvalues of Casimir operators for the groups G_2 and R_7. The T, M, and P terms denote additional corrections due to three-body interactions, relativistic effects (spin–spin, spin–other-orbit), and configuration interactions. A comprehensive description of all these terms is given in Ref. 26.

The influence of the crystal field can be accounted for by a crystal-field potential defined by

$$\mathcal{H}_{\mathrm{CF}} = \sum_{k,q,i} B_q^k C_q^{(k)}(i), \tag{6}$$

where the i summation is over all electrons of interest, B_q^k are the crystal-field parameters, and $C_q^{(k)}$ are the components of tensor operators $\mathbf{C}^k$ that transform like spherical harmonics.

The parameters in the complete Hamiltonian can be derived for a specific system from a fit to experimentally determined energy levels for this system. For SBN:Eu, we derived the experimental energy levels from the transitions measured in absorption and emission using a least-square-fit approach. Generally all parameters of the free-ion and the crystal-field Hamiltonian could be varied to get an optimal fit to the experimental data. To reduce the degrees of freedom, however, we restricted the fit to the crystal-field parameters and kept fixed values for the free-ion parameters that were taken from literature.[27] For the calculation of the fit, we used the *f -shell* routines provided by M. F. Reid. For the symmetry of the crystal field, we assumed C_{2v} (symmetry of the dominant structural site B1, see Sec. IV).

Our results are summarized in Table II, where all fit parameters are listed, and in Table III, where the values for the experimentally determined and for the fitted energies are presented.

The standard deviation STD for our fit was

$$\mathrm{STD} = \left[\sum_{i=1}^{m} \frac{(\Delta E_i)^2}{m-p} \right]^{1/2} = 23 \ \mathrm{cm}^{-1}, \tag{7}$$

where ΔE_i are the differences between experimental and fitted energies, m is the number of experimental energy levels included in the fit, and p is the number of varied parameters.

TABLE II. Fit parameters (free-ion and crystal-field parameters) for Eu^{3+} in SBN for the dominant structural site B1 with C_{2v} symmetry. The values in brackets are kept constant during the fit (taken from literature, see text). Values in parentheses denote errors in the respective parameters.

Parameter	Value [cm^{-1}]
E_{avg}	63 861 (1)
F^2	82 877 (3)
F^4	[60 937]
F^6	[41 121]
α	[20.16]
β	[−566.9]
γ	[1500]
ζ	[1328]
T^2	[300]
T^3	[40]
T^4	[60]
T^6	[−300]
T^7	[370]
T^8	[320]
M_{tot}	[2.1]
P_{tot}	[360]
B_0^2	−247 (14)
B_2^2	−287 (10)
B_0^4	−1061 (24)
B_2^4	−188 (17)
B_4^4	−353 (20)
B_0^6	−504 (35)
B_2^6	−85 (15)
B_4^6	−1094 (25)
B_6^6	−78 (25)

C. Additional site

As shown in Sec. IIIC, a series of comparably sharp lines is found in the luminescence spectra under *special* excitation conditions (Fig. 7). *Special* conditions mean low temperature and excitation with 532 nm laser light. A closer inspection of the luminescence spectra at room-temperature and *normal* excitation conditions (Fig. 5) shows that these lines also show up as a marginal shoulder at the high-energy side of the $^5D_0 \Rightarrow {}^7F_1$ band. From these facts an additional structural site must be concluded, which, however, is only marginally occupied.

Only the four sharp lines shown in Fig. 7 could be identified in the spectra to be connected with the additional site. The energies derived from these lines are listed in Table IV in comparison to the energies of the *main* sites.

The properties of the additional site can be summarized as follows:

(1) The degeneracy of the $^7F_1$ level is lifted, the transition $^5D_0 \Rightarrow {}^7F_1$ shows three lines.

(2) The splitting of the $^7F_1$ level is moderate, which means a minor effect of the crystal field.

(3) The energy of the $^5D_0$ level is typical for ionic environments, i.e., large Eu–O distances.[28,29]

(4) The small half width of the bands hints on a single site without inhomogeneous broadening, i.e., experiencing an environment, which is identical throughout the crystal lattice.

Taking into account all properties listed, one must conclude on A2 as an additional site. At this site, partly occupied by Sr or Ba, there are the largest distances to the surrounding oxygen ions. A1, albeit also exhibiting large distances to the oxygens, can be excluded as the $^7F_1$ degeneracy should only be partially lifted (due to the C_4 symmetry only two levels should be expected, see Table I). Furthermore, concerning the crystal structure (see discussion above), the A sites are surrounded by a second-nearest-neighbor shell, which consists of Nb-filled oxygen octahedra. This environment should not show any variation through the crystal lattice. So the narrow linewidth found is also compatible with the A2 site.

TABLE III. Experimental and fitted energy levels of Eu^{3+} in SBN for C_{2v} symmetry.

Nr.	Term	E_{exp} [cm^{-1}]	E_{fit} [cm^{-1}]
1	$^7F_0$	0.0	−0.32
2	$^7F_1$	281.0	304.64
3	$^7F_1$	355.0	359.85
4	$^7F_1$	455.0	482.48
5	$^7F_2$	948.0	927.69
6	$^7F_2$		985.17
7	$^7F_2$	1039.0	1026.76
8	$^7F_2$	1089.0	1092.05
9	$^7F_2$	1221.0	1208.46
10	$^7F_3$	1813.0	1819.43
11	$^7F_3$		1862.69
12	$^7F_3$	1873.0	1884.24
13	$^7F_3$		1905.27
14	$^7F_3$	1933.0	1927.88
15	$^7F_3$	1992.0	1975.42
16	$^7F_3$	2051.0	2037.00
17	$^7F_4$		2602.72
18	$^7F_4$	2799.0	2803.70
19	$^7F_4$	2804.0	2838.34
20	$^7F_4$		2847.80
21	$^7F_4$	2869.0	2872.56
22	$^7F_4$		3009.81
23	$^7F_4$	3048.0	3051.54
24	$^7F_4$		3052.50
25	$^7F_4$		3103.48
26	$^7F_5$		3802.43
27	$^7F_5$		3816.08
28	$^7F_5$	3846.0	3894.40
29	$^7F_5$		3922.40
30	$^7F_5$		3957.93
31	$^7F_5$		3962.82
32	$^7F_5$	4016.0	4024.36
33	$^7F_5$	4050.0	4039.41
34	$^7F_5$	4119.0	4138.99
35	$^7F_5$		4166.95
36	$^7F_5$		4178.34
37	$^7F_6$	4897.0	4930.81
38	$^7F_6$		4938.27
39	$^7F_6$	4941.0	4938.75
40	$^7F_6$	4949.0	4950.06
41	$^7F_6$		5020.08
42	$^7F_6$		5020.20
43	$^7F_6$		5071.39
44	$^7F_6$	5089.0	5099.30
45	$^7F_6$	5168.0	5164.53
46	$^7F_6$		5181.60
47	$^7F_6$	5203.0	5207.16
48	$^7F_6$		5356.43
49	$^7F_6$	5339.0	5357.04
50	$^5D_0$	17 247.0	17 189.00
51	$^5D_1$		18 942.41
52	$^5D_1$	18 986.0	18 961.54
53	$^5D_1$	19 015.0	19 001.94
54	$^5D_2$		21 426.73
55	$^5D_2$		21 447.87
56	$^5D_2$		21 467.62
57	$^5D_2$	21 473.0	21 472.76
58	$^5D_2$	21 482.0	21 478.11
59	$^5D_3$	24 301.0	24 309.50
60	$^5D_3$		24 309.58
61	$^5D_3$		24 312.94
62	$^5D_3$		24 339.51
63	$^5D_3$		24 343.67
64	$^5D_3$	24 355.0	24 356.45
65	$^5D_3$		24 371.40
66	$^5L_6$		24 985.56
67	$^5L_6$		25 007.01
68	$^5L_6$		25 013.66
69	$^5L_6$		25 023.58
70	$^5L_6$		25 042.80
71	$^5L_6$		25 073.13
72	$^5L_6$	25 189.0	25 227.65
73	$^5L_6$		25 229.31
74	$^5L_6$		25 302.07
75	$^5L_6$		25 309.79
76	$^5L_6$		25 316.10
77	$^5L_6$		25 331.69
78	$^5L_6$	25 380.0	25 349.90
79	$^5G_2$		25 933.90
80	$^5L_7$		26 017.50
81	$^5L_7$		26 030.86
82	$^5G_2$		26 037.73
83	$^5L_7$		26 084.82
84	$^5G_2$		26 090.92
85	$^5L_7$		26 098.58
86	$^5L_7$		26 099.20
87	$^5L_7$		26 159.21
88	$^5L_7$		26 190.68
89	$^5L_7$		26 193.93
90	$^5L_7$		26 250.88
91	$^5L_7$		26 261.43
92	$^5L_7$		26 271.95
93	$^5L_7$		26 310.60
94	$^5G_3$		26 319.51
95	$^5G_3$		26 319.82
96	$^5G_3$		26 347.42
97	$^5G_3$	26 413.0	26 400.33
98	$^5L_7$		26 401.49
99	$^5G_3$	26 455.0	26 429.90
100	$^5G_3$		26 429.94
101	$^5L_7$		26 440.21
102	$^5G_6$		26 463.10
103	$^5G_2$		26 466.89
104	$^5L_7$		26 471.75
105	$^5L_7$		26 483.50
106	$^5G_4$	26 511.0	26 519.02
107	$^5G_4$		26 524.83
108	$^5G_5$	26 539.0	26 544.69
109	$^5G_5$		26 545.04
110	$^5G_5$	26 560.0	26 546.84

TABLE IV. Energies of the $^7F_1$ and the $^5D_0$ levels for Eu^{3+} at the dominant site(s) (Site I) and at the additional site (Site II).

Term	E_{exp} [cm^{-1}]	
SLJ	Site I	Site II
$^7F_0$	0	0
$^7F_1$	281	197
$^7F_1$	355	233
$^7F_1$	455	263
$^5D_0$	17 247	17 277

Thus, the major part of Eu^{3+} occupies B1 and B2 sites while a minor part—not exceeding some percent—is found on A2 sites.

D. Judd–Ofelt analysis

According to the theory of Judd[30] and Ofelt,[31] the line strengths for electric-dipole transitions can be referred to three intensity parameters Ω_2, Ω_4, and Ω_6, the so-called Judd–Ofelt parameters. The line strength for a transition from an initial multiplet J to a final one J' is given by

$$S_{JJ'}^{\mathrm{ed,cal}} = \sum_{t=2,4,6} \Omega_t |\langle 4f^n[\alpha SL]J||U^{(t)}||4f^n[\alpha' S'L']J'\rangle|^2. \quad (8)$$

In Eq. (8), the $|\langle\|U^{(t)}\|\rangle|^2$ are the squared reduced matrix elements of the unit tensor operators $U^{(t)}$ connecting the initial and final multiplets. Values for these matrix elements have been calculated by Carnall *et al.*[18]

On the other hand, experimental line strengths can be derived from absorption measurements

$$S_{JJ'}^{\mathrm{ed,exp}} = \frac{3ch\epsilon_0(2J+1)n}{2\pi\bar{\lambda}e^2N}\left[\frac{9}{(n^2+2)^2}\right]\int \alpha(\lambda)d\lambda. \quad (9)$$

Here, the integral has to be calculated over the respective absorption band with $\bar{\lambda}$ being the mean wavelength of the band. N is the concentration of Eu^{3+} ions in the crystal, effective for the respective transition, n is the refractive index, and c, h, ϵ_0, and e are the usual constants.

In optically anisotropic crystals, several properties depend on the light polarization; thus, for the absorbance integral and for n, the values for the respective polarization have to be used, resulting in polarization-dependent values S and Ω. SBN is optically uniaxial; thus, one has to distinguish between two light polarizations: the ordinary one parallel to the crystallographic x-y plane and the extraordinary one parallel to the crystallographic z axis. As *effective* values for S and Ω, the appropriate spatial averages may be used.

For the case of Eu^{3+}, an additional slight complication has to be included. Absorption bands are starting from $^7F_0$ and from $^7F_1$ levels; the energy difference between these levels is approximately 350 cm^{-1}, thus their thermal occupancy has to be taken into account when calculating the relevant Eu^{3+} concentration N in the crystals.

Equations (8) and (9) define a system of linear equations for the Ω_t, which is usually overdetermined. It can be solved by applying a conventional least-square-fit solution scheme. Using our absorption spectra, appropriate refractive indices,[20] and the matrix elements calculated by Carnall *et al.*,[18] we calculated the Ω_t for different concentrations of Eu^{3+}. The values derived did not show any expressed dependence on the concentration, which proves that—up to our highest concentrations—no interaction effects between different Eu^{3+} ions take place. The Ω values for the relevant light polarizations are summarized in Table V.

TABLE V. Judd–Ofelt parameters Ω for Eu^{3+} in strontium barium niobate. E denotes the direction of the light polarization parallel to the crystallographic x-y plane (ordinary) or parallel to the crystallographic z axis (extraordinary).

	Judd–Ofelt		
Parameter	$E\|X,Y$	$E\|Z$	Effective
Ω [10^{-24} m^2]			
Ω_2	1.5	3.2	2.1
Ω_4	3.1	5.2	3.8
Ω_6	0.67	0.53	0.62

E. Spontaneous emission rates

Using the Judd–Ofelt parameters and the appropriate transition matrix elements, the spontaneous emission rates for the transitions starting at the $^5D_0$ level can be calculated. These transition rates determine the radiative lifetime of the starting level. For electric-dipole transitions the spontaneous emission rate can be written as

$$A_{JJ'}^{\mathrm{ed}} = \frac{16\pi^3e^2}{3\epsilon_0h(2J+1)\bar{\lambda}^3}\frac{n(n^2+2)^2}{9}S_{JJ'}^{\mathrm{ed}}, \quad (10)$$

with $S_{JJ'}^{\mathrm{ed}}$, as defined in Eq. (8).

The squared transition matrix elements can be taken from literature, according to Refs. 32 and 33. The squared matrix elements for the electric-dipole-allowed transitions are

$$|\langle {}^5D_0||U^{(2)}||{}^7F_2\rangle|^2 = 0.0032,$$

$$|\langle {}^5D_0||U^{(4)}||{}^7F_4\rangle|^2 = 0.0023,$$

$$|\langle {}^5D_0||U^{(6)}||{}^7F_6\rangle|^2 = 0.00025.$$

Using these values and the Judd–Ofelt parameters derived in the previous section, the spontaneous emission rates for the relevant electric-dipole transitions could be calculated. The values for the magnetic-dipole transition $^5D_0 \Rightarrow {}^7F_1$ were derived from a comparison of the respective bands in the luminescence spectra with those for the $^5D_0 \Rightarrow {}^7F_2$ electric-dipole transition. All emission rates thus determined are summarized in Table VI.

The total effective spontaneous emission rate for the $^5D_0$ level is the sum over all contributing transitions

TABLE VI. Calculated spontaneous emission rates for Eu^{3+} in strontium barium niobate. ED denotes electric dipole transition while MD denotes magnetic-dipole transition.

Transition $J \Rightarrow J'$	Spontaneous emission rate $A_{JJ'}^{ed}$, $A_{JJ'}^{md}$ [s^{-1}]		
	$E\|\|X,Y$	$E\|\|Z$	Effective
ED: $^5D_0 \Rightarrow {}^7F_2$	211	451	291
ED: $^5D_0 \Rightarrow {}^7F_4$	215	361	264
ED: $^5D_0 \Rightarrow {}^7F_6$	3.4	2.7	3.2
MD: $^5D_0 \Rightarrow {}^7F_1$	134	242	170

$$A_{\text{total}} = \sum_{J'} A_{JJ'} = 728 \ \text{s}^{-1}. \tag{11}$$

A_{total} defines the radiative lifetime τ_{rad} of the $^5D_0$ level to $\tau_{\text{rad}} = 1.4$ ms. Comparing this value with the measured total lifetime of approximately 1 ms yields the quantum efficiency for the radiative transitions starting at the $^5D_0$ level to be about 70%.

VI. SUMMARY

Strontium barium niobate crystals with different amount of europium doping have been grown from the congruently melting composition. Absorption and emission spectra show that different structural sites are occupied. The main features of the spectra can be explained by one major occupied site, B1. Additional features, however, show that the B2 site must also be occupied. Thus Eu^{3+} ions mainly substitute Nb ions in SBN. Extremely narrow, rather weak lines found in the low-temperature spectra, however, strongly hint on a minor occupation of A2 sites, too.

We could, furthermore, show that europium doping strongly affects the transition temperature from the low-temperature ferroelectric to the high-temperature paraelectric phase of SBN. This transition temperature decreases linearly from 350 K for undoped SBN to approximately 300 K for a doping level of 1.2 mol % europium. On the other hand, the phase-transition influences the total lifetime: a decrease from approximately 1 ms in the ferroelectric phase to 0.3 ms at temperatures approximately 100 K beyond the phase-transition temperature is found.

The crystal-field parameters for the symmetry of the B1 site (C_{2v}) were derived from a fit to the experimental data. The fit shows that the data are well compatible with C_{2v} symmetry. The Judd–Ofelt parameters were determined from a least-squares evaluation of several absorption bands. From these parameters the spontaneous emission rates are calculated, yielding a total radiative emission rate for the $^5D_0$ level of 728 s^{-1}, corresponding to a radiative lifetime of 1.4 ms and—with the total lifetime of 1 ms—a radiative quantum efficiency of approximately 70%.

ACKNOWLEDGMENTS

Financial support from the Deutsche Forschungsgemeinschaft through the Graduate College *Nonlinearities of Optical Materials* is gratefully acknowledged. The authors are grateful to M. F. Reid for providing the *f*-shell program and helpful hints for its application.

*klaus.betzler@uni-osnabrueck.de
†On leave from Departamento de Física, Universidad Autónoma Metropolitana, Iztapalapa, P.O. Box 55–534, 09340 México, Distrito Federal, México

[1] A. M. Glass, J. Appl. Phys. **40**, 4699 (1969).
[2] R. R. Neurgaonkar, M. H. Kalisher, T. C. Lim, E. J. Staples, and K. L. Keester, Mater. Res. Bull. **15**, 1235 (1980).
[3] R. R. Neurgaonkar, W. K. Cory, J. R. Oliver, E. J. Sharp, M. J. Miller, G. L. Wood, W. W. Clark III, A. G. Mott, G. J. Salamo, and B. D. Monson, Proc. SPIE **1148**, 2 (1989).
[4] F. Kahmann, J. Höhne, R. Pankrath, and R. A. Rupp, Phys. Rev. B **50**, 2474 (1994).
[5] H. Y. Zhang, X. H. He, Y. H. Shih, and L. Yan, J. Mod. Opt. **669**, 6613 (1994).
[6] A. S. Kewitsch, M. Segev, A. Yariv, G. J. Salamo, T. W. Towe, E. J. Sharp, and R. R. Neurgaonkar, Appl. Phys. Lett. **64**, 3068 (1994).
[7] M. Wesner, C. Herden, R. Pankrath, D. Kip, and P. Moretti, Phys. Rev. E **64**, 036613 (2001).
[8] M. Ulex, R. Pankrath, and K. Betzler, J. Cryst. Growth **271**, 128 (2004).
[9] C. David, T. Granzow, A. Tunyagi, M. Wöhlecke, T. Woike, K. Betzler, M. Ulex, M. Imlau, and R. Pankrath, Phys. Status Solidi A **201**, R49 (2004).
[10] T. Granzow, T. Woike, W. Rammensee, M. Wöhlecke, M. Imlau, and R. Pankrath, Phys. Status Solidi A **197**, R2 (2003).
[11] J. J. Romero, D. Jaque, J. García Solé, and A. A. Kaminskii, Appl. Phys. Lett. **78**, 1961 (2001).
[12] N. C. Giles, J. L. Wolford, G. J. Edwards, and R. Uhrin, J. Appl. Phys. **77**, 976 (1995).
[13] M. H. Li, X. W. Xu, T. C. Chong, H. Kumagai, and M. Hirano, Ferroelectrics **230**, 529 (1999).
[14] M. H. Li, T. C. Chong, X. W. Xu, and H. Kumagai, J. Cryst. Growth **225**, 479 (2001).
[15] H. Liu, G. K. Liu, S. T. Li, J. V. Beitz, and F. E. Fernandez, J. Appl. Phys. **91**, 129 (2002).
[16] M. Bettinelli, A. Speghini, A. Ródenas, P. Molina, M. de la O Ramírez, B. Capote, D. Jaque, L. E. Bausá, and J. G. Solé, J. Lumin. **122-123**, 307 (2007).
[17] S. Kapphan, B. Pedko, V. Trepakov, M. Savinov, R. Pankrath, and I. Kislova, Radiat. Eff. Defects Solids **157**, 1033 (2002).
[18] W. T. Carnall, P. R. Fields, and K. Rajnak, J. Chem. Phys. **49**, 4450 (1968).
[19] G. H. Dieke, *Spectra and Energy Levels of Rare Earth Ions in Crystals* (Interscience, New York/Wiley, New York, 1968).
[20] C. David, A. Tunyagi, K. Betzler, and M. Wöhlecke, Phys. Status Solidi B **244**, 2127 (2007).
[21] H. Najafov, Y. Sato, S. Ohshio, S. Iida, and H. Saitoh, Jpn. J.

Appl. Phys., Part 1 **42**, 6441 (2003).
[22] P. B. Jamieson, S. C. Abrahams, and J. L. Bernstein, J. Chem. Phys. **48**, 5048 (1968).
[23] T. S. Chernaya, B. A. Maksimov, I. V. Verin, L. I. Ivleva, and V. I. Simonov, Crystallogr. Rep. **42**, 375 (1997).
[24] S. Podlozhenov, H. A. Graetsch, J. Schneider, M. Ulex, M. Wöhlecke, and K. Betzler, Acta Crystallogr., Sect. B: Struct. Sci. **62**, 960 (2006).
[25] M. Daldosso, A. Speghini, P. Ghigna, M. de la O. Ramirez, D. Jaque, L. E. Bausá, J. G. Solé, and M. Bettinelli, J. Alloys Compd. **451**, 12 (2008).
[26] G. Liu, in *Spectroscopic Properties of Rare Earth in Optical Materials*, Springer Series in Material Sciences No. 83, edited by G. Liu and B. Jacquier (Springer-Verlag, Berlin, 2005), pp. 1–94.
[27] W. T. Carnall, G. L. Goodman, K. Rajnak, and R. S. Rana, J. Chem. Phys. **90**, 3443 (1989).
[28] J. A. Capobianco, P. P. Proulx, and N. Raspa, Chem. Phys. Lett. **161**, 151 (1989).
[29] P. Caro, O. Beaury, and E. Antic, J. Phys. (Paris) **37**, 671 (1976).
[30] B. R. Judd, Phys. Rev. **127**, 750 (1962).
[31] G. S. Ofelt, J. Chem. Phys. **37**, 511 (1962).
[32] W. T. Carnall, H. Crosswhite, and H. M. Crosswhite, *Energy Level Structure and Transition Probabilities in the Spectra of the Trivalent Lanthanides in Lanthanum Fluoride* (Argonne National Laboratory, Argonne, IL, 1978).
[33] L. Liu and X. Chen, Nanotechnology **18**, 255704 (2007).